Supplementary Information

Revealing the atomic-scale configuration modulation effect of boron dopant on carbon layers for H_2O_2 production

Xuyun Lu,[#a] Xiaozhi Liu,[#b] Jianing Li,[a] Ye Yao,[a] Zhangyu Ma,[a] Yanan Chang,[a] Jianchun Bao[a] and Ying Liu[a]*

[a]School of Chemistry and Materials Science, Nanjing Normal University, Nanjing 210023, China. Email: liuyingg@njnu.edu.cn

[b]Beijing National Laboratory for Condensed Matter Physics, Institute of Physics, Chinese Academy of Sciences, Beijing 100190, China

#These authors contribute to this work equally.

Experimental Section/Methods

1. Chemicals

Nickel Chloride ($NiCl_2$), nitrilotriacetic acid (NTA) and Nafion (5.0 wt%) were purchased from Alfa Aesar in analytical grade (AR). Boric acid (H_3BO_3), potassium hydroxide (KOH), sodium sulfocyanate (NaSCN), 2-propanol and absolute ethyl alcohol were obtained from Sinopharm Chemical Reagent Co., Ltd. Ceric sulfate ($Ce(SO_4)_2$) was bought from Aladdin Industrial Corporation. Ultrapure water was obtained from a Millipore water purification system (≥18.25 MΩ cm, Millipore SAS Corporation, France). Unless otherwise stated, all the above chemicals were used directly without further purification.

2. Synthesis

Synthesis of Ni@B,N-C hollow nanorods

The Ni@B,N-C hollow nanorods were synthesized in two steps: Firstly, $NiCl_2$ (6 mmol) and NTA (3 mmol) were dissolved in the mixture of 2-propanol (10 mL) and ultrapure water (30 mL) under strong ultrasonic for about 30 min to obtain a homogenous green solution. Then the solution was transferred to a Teflon-lined stainless autoclave (100 mL) and sealed for 6 h solvothermal reaction under 180 °C. After the reaction, the generated green precipitate was centrifuged and separated with ultrapure water and 2-propanol, followed by cryodesiccated overnight to obtain the Ni-NTA precursor. Secondly, the Ni-NTA precursor (50 mg) was grinded with H_3BO_3 (250 mg), and the obtained solid mixture was annealed treatment in a tubular furnace under N_2 atmosphere at 500 °C for 2 h. Related heating rate is 5 °C min^{-1}. After naturally cooled down to room temperature, the powder was washed with ultrapure water to remove some possible impurities (such as B_2O_3), and then centrifuged, separated, dried and collected for subsequent characterization and tests.

Synthesis of Ni@N-C hollow nanorods

The synthetic procedure of Ni@N-C hollow nanorods was similar to that for Ni@B,N-C hollow nanorods, but H_3BO_3 was not added.

Synthesis of Ni nanoparticles

The Ni nanoparticles were obtained from Ni@B,N-C product with further treatment. Specifically, the Ni@B,N-C powder was first annealed at 500 °C under air atmosphere for 2 h

to remove the carbon shell. Thereafter, the as-obtained powder was further annealed at 500 °C under H_2/Ar atmosphere for 2 h to get the desired Ni nanoparticles.

3. Characterization

Transmission electron microscopy (TEM) images were recorded on JEM-200CX microscope (Japan) with an accelerating voltage of 200 kV. The powder X-ray diffraction (XRD) patterns were collected on a D/max 2500VL/PC diffractometer (Japan) equipped with graphite-monochromatized Cu Kα radiation (λ = 1.54060 Å), and corresponding scan range (2θ) was 5° to 90°. X-ray photoelectron spectroscopy (XPS) measurements were performed on a scanning X-ray microprobe (PHI 5000 Versa, ULACPHI, Inc.) with Al Kα radiation. All energies were calibrated using the C 1s peak (binding energy = 284.8 eV) as standard. The X-ray absorption fine structure (XAFS) measurements were carried out at 21A X-ray nano-diffraction beamline of Taiwan Photon Source (TPS), National Synchrotron Radiation Research Center (NSRRC). Fourier transform infrared (FTIR) spectra were recorded on Tensor 27 (Bruker, Germany) at room temperature. The Raman spectra were recorded on a JY HR 800 (France) instrument with 532 nm laser source. UV-vis diffuse reflectance spectra were investigated on Cary 5000 UV-vis spectrophotometer (Varian, America). The O_2 temperature-programmed desorption (O_2-TPD) detection was conducted on a TP-5080 chemisorption instrument. Before tests, the sample (0.1 g) was first pretreated in He gas at 200 °C for 2 h. Then O_2/He (50 mL/min) was absorbed at 50 °C for 1 h, followed by He gas to remove weakly adsorbed species. Finally, the system temperature was increased to 700 °C at a rate of 10 °C min^{-1} for O_2 desorption. The electrochemical impedance spectroscopy (EIS) tests were conducted on CHI 660E workstation at a frequency range of 10^6 to 10^{-1} Hz in 0.1 M KOH.

4. Electrochemical measurement

The electrochemical $2e^-$ ORR tests were carried out on a CHI 760E electrochemical station with a standard three-electrode system in 0.1 M KOH electrolyte. Graphite rod, Hg/HgO electrode and rotating ring-disk electrode (RRDE) loaded with catalyst were used as the counter electrode, reference electrode and working electrode, respectively. To prepare the working electrode, 1.5 mg catalyst was first dispersed in the mixture of 480 μL of ethanol, 480 μL of ultrapure water and 40 μL of Nafion solution (5 wt%) under strong ultrasonic for about 30 min. Then 5 μL of above catalyst ink was pipetted onto the surface of RRDE and naturally dried to obtain the catalyst modified working electrode (mass loading: 30 μg cm^{-2}).

Before electrochemical tests, the 0.1 M KOH electrolyte was first bubbled with high purity O_2 for about 30 min. Then the modified working electrode were pretreated by performing cyclic voltammetry (CV) cycling for several cycles until stable to remove any possible surface contamination. Subsequently, linear sweep voltammetry (LSV) tests were conducted with an electrode rotating speed of 1600 rpm, potential window of -0.9 to 0.1 V (vs. Hg/HgO) and scan rate of 10 mV s^{-1}. To detect and quantify the production of H_2O_2, the platinum ring potential was fixed at 1.28 V (vs. RHE) during the entire tests. All ORR current was corrected by subtracting the current measured in N_2-saturated electrolyte from that in O_2-saturated ones. All potentials were referenced to reversible hydrogen electrode (RHE) values using the following equation $E(RHE) = E_{Hg/HgO} + 0.098 + 0.059$ pH.

The selectivity of H_2O_2 was calculated according to equation (1):

$$H_2O_2 \text{ selectivity } (\%) = 200\ (I_r/N) / (|I_d| + I_r/N) \qquad (1)$$

The number of electron transfer number (n) could be calculated by equation (2):

$$n = 4|I_d| / (|I_d| + I_r/N) \qquad (2)$$

where I_d, I_r and N stand for the disk current, ring current, and current collection efficiency (0.37) of the Pt ring, respectively.

H_2O_2 synthesis and concentration measurement

The mass synthesis of H_2O_2 was carried out in an H-cell electrolyzer with two chambers separated by Nafion 117 membrane. Graphite rod and Hg/HgO electrode were used as the counter electrode and reference electrode, respectively. Whereas carbon fiber cloth (1 x 1 cm^2) coated with catalyst (1 mg cm^{-2}) was used as the working electrode. All H_2O_2 yield tests were conducted in 0.1 M KOH electrolyte (30 mL with continuously O_2 bubbling) at 0.2 V for 3 h. To determine the concentration of H_2O_2, 20 μL of above electrolyte was taken out from the cathode chamber periodically and added to 8 mL $Ce(SO_4)_2$ solution (0.2 mM, prepared by dissolving 16.6 mg $Ce(SO_4)_2$ in 250 mL of 0.5 M sulfuric acid solution). Subsequently, the H_2O_2 concentration was measured by a traditional cerium sulfate titration method based on the following equation:

$$2Ce^{4+}(\text{yellow}) + H_2O_2 = 2Ce^{3+}(\text{colorless}) + 2H^+ + O_2 \qquad (3)$$

where the concentration of residual Ce^{4+} was calculated from the intensity of the UV-vis absorption peak at 317 nm.

The faradaic efficiency (FE) for H_2O_2 generation was calculated as follows:

$$FE\% = \frac{C_{H2O2}\, x\, V_{cell} x\, 2\, x\, F}{I\, x\, t}\, x\, 100\ \% \qquad (4)$$

where C_{H2O2} is the H_2O_2 concentration in the electrolyte (mol L^{-1}), V_{cell} is the volume of electrolyte in the cathode chamber, F is the faraday constant (96485 C mol^{-1}), I is the operating current and t is test time.

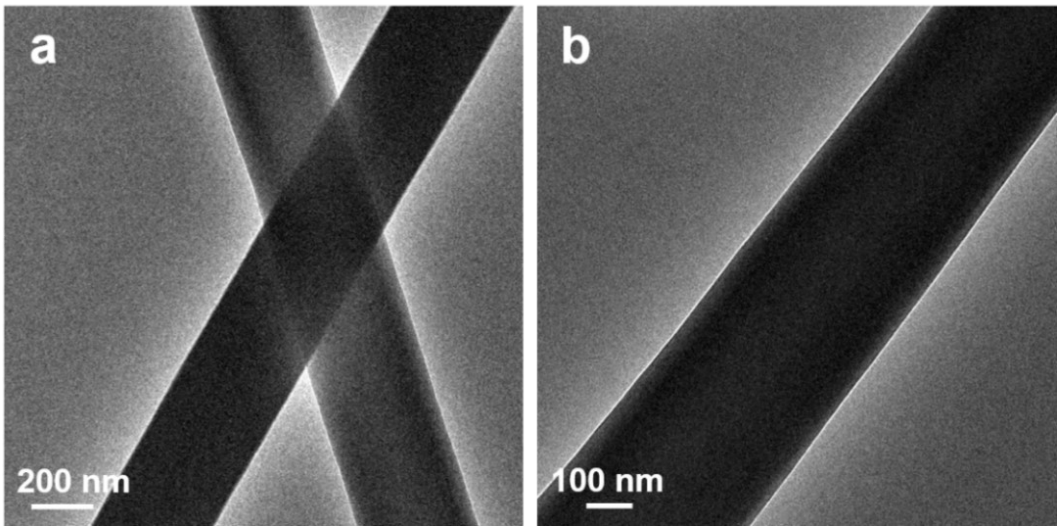

Fig. S1 (a, b) TEM images of the Ni-NTA complex intermediate.

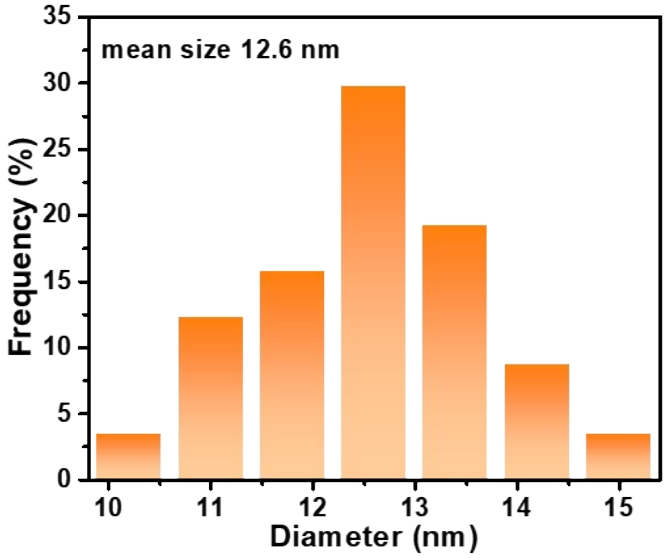

Fig. S2 Diameter distribution diagram of the Ni nanoparticles in Ni@B,N-C NHs.

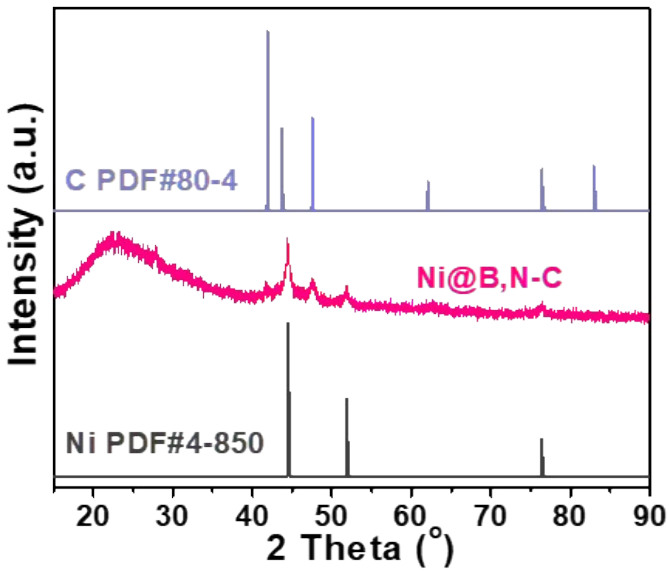

Fig. S3 XRD pattern of the Ni@B,N-C NHs.

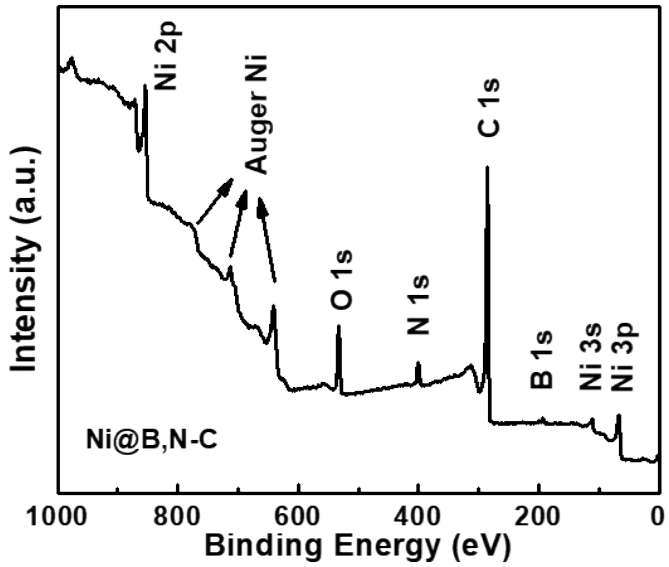

Fig. S4 XPS survey spectra of the Ni@B,N-C NHs.

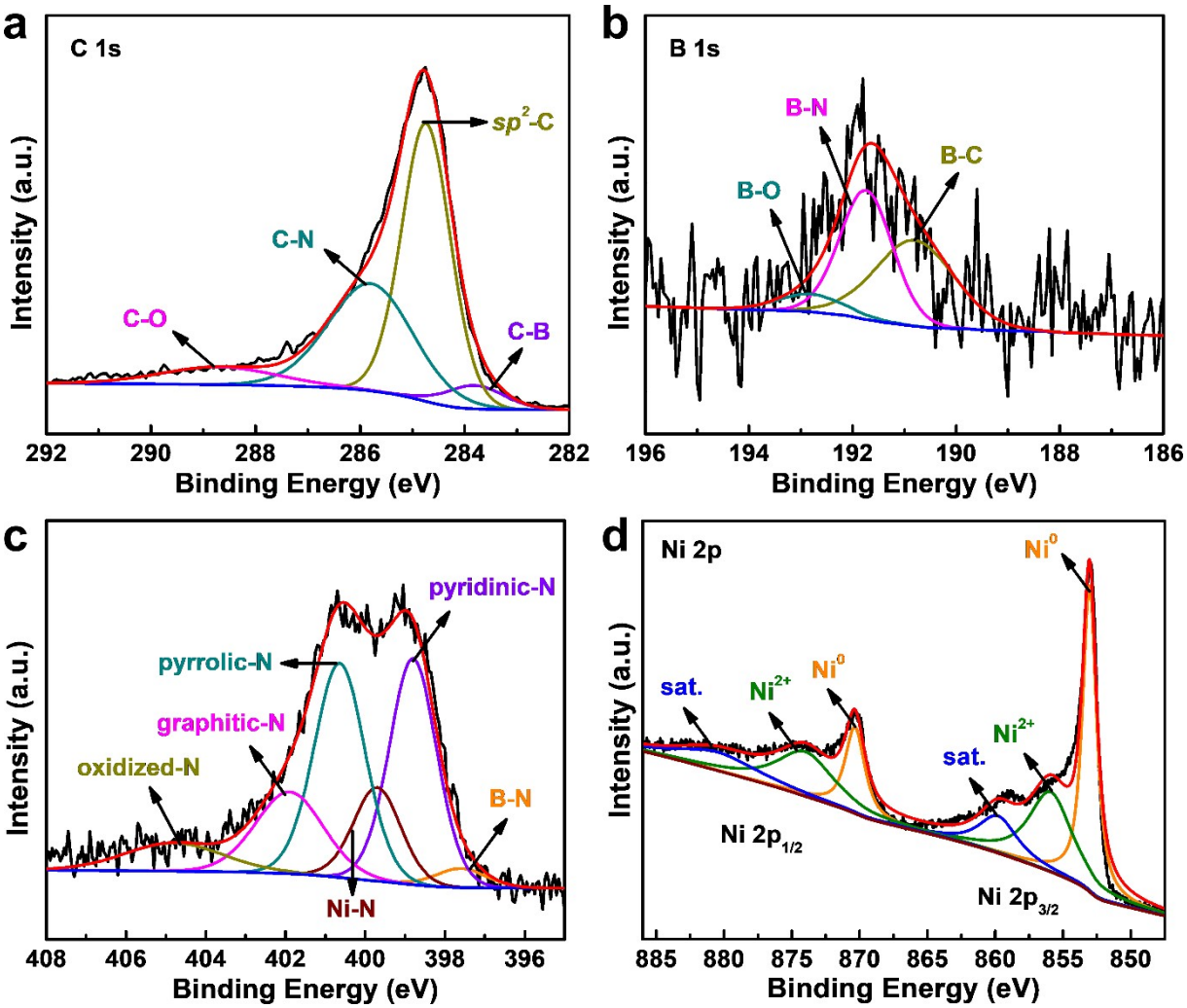

Fig. S5 High-resolution (a) C 1s, (b) B 1s, (c) N 1s, and (d) Ni 2p XPS spectra for the Ni@B,N-C NHs.

To examine the chemical state in the surface of the Ni@B,N-C NHs, X-ray photoelectron spectroscopy (XPS) was performed. Fig. S5a displays the fine XPS spectrum of C 1s in Ni@B,N-C NHs, which can be deconvoluted into four peaks centered at 283.8, 284.8, 285.8, and 288.7 eV, corresponding to C-B, sp^2-C, C-N, and C-O, respectively. The presence of C-B and C-N bonds signifies the doping of B and N in the carbon skeleton. This can be further proved by the analysis of B 1s and N 1s XPS spectra. As shown in Fig. S5b, the fine B 1s spectrum can be deconvoluted into three peaks, and the two peaks at lower binding energies correspond to B-C (190.8 eV) and B-N (191.7 eV), respectively, in the B and N co-doped carbon matrix, while the last peak results from B-O (192.8 eV). In the high-resolution N 1s spectrum, the four deconvoluted peaks at 397.6, 398.9, 400.6, and 401.8 eV can be assigned to B-N, pyridinic-N, pyrrolic-N, and graphitic-N in order (Fig. S5c). Whereas the last two small peaks at 399.7 eV and 404.8 eV are associated with Ni-N and N-oxides, respectively. The

existence of the Ni-N bond herein should originate from the incorporation of monodispersed Ni species in the B and N co-doped carbon matrix, which is in good accordance with the HADDF-STEM image shown above. Fig. S5d displays the fine Ni 2p XPS spectrum, where the two dominant peaks located at 853.1 ($2p_{3/2}$) and 870.4 eV ($2p_{1/2}$) are ascribed to metallic Ni, and the other two peaks at 856.1 ($2p_{3/2}$) and 874.1 eV ($2p_{1/2}$) are assigned to Ni^{2+}. This indicates that the Ni species in Ni@B,N-C NHs mainly exist as metallic Ni (0) and Ni single atoms.

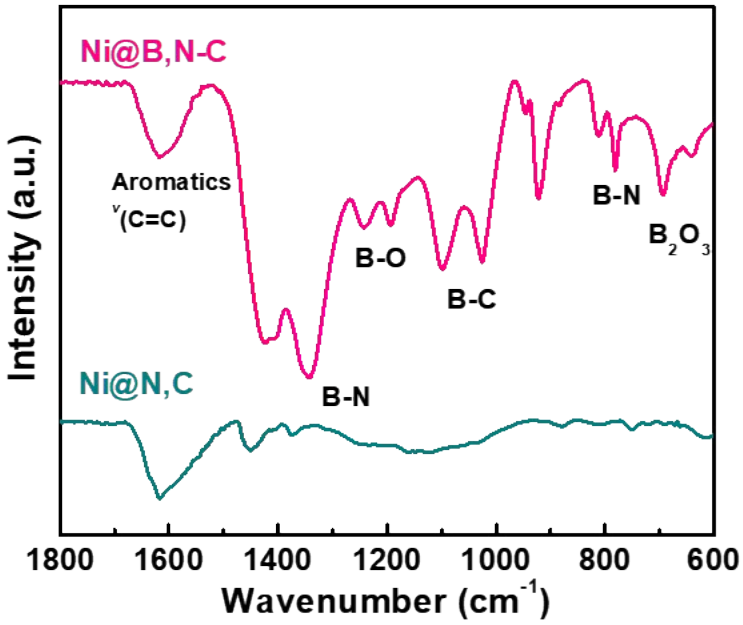

Fig. S6 Fourier transform infrared spectra of the Ni@B,N-C and Ni@N-C NHs.

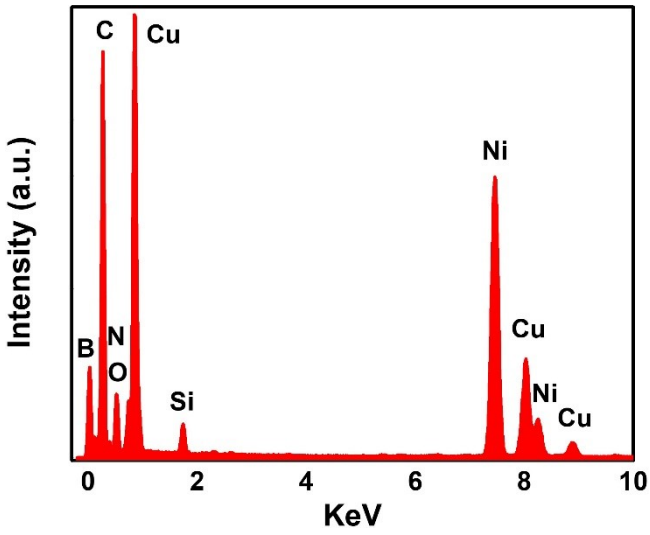

Fig. S7 EDS pattern of the Ni@B,N-C NHs.

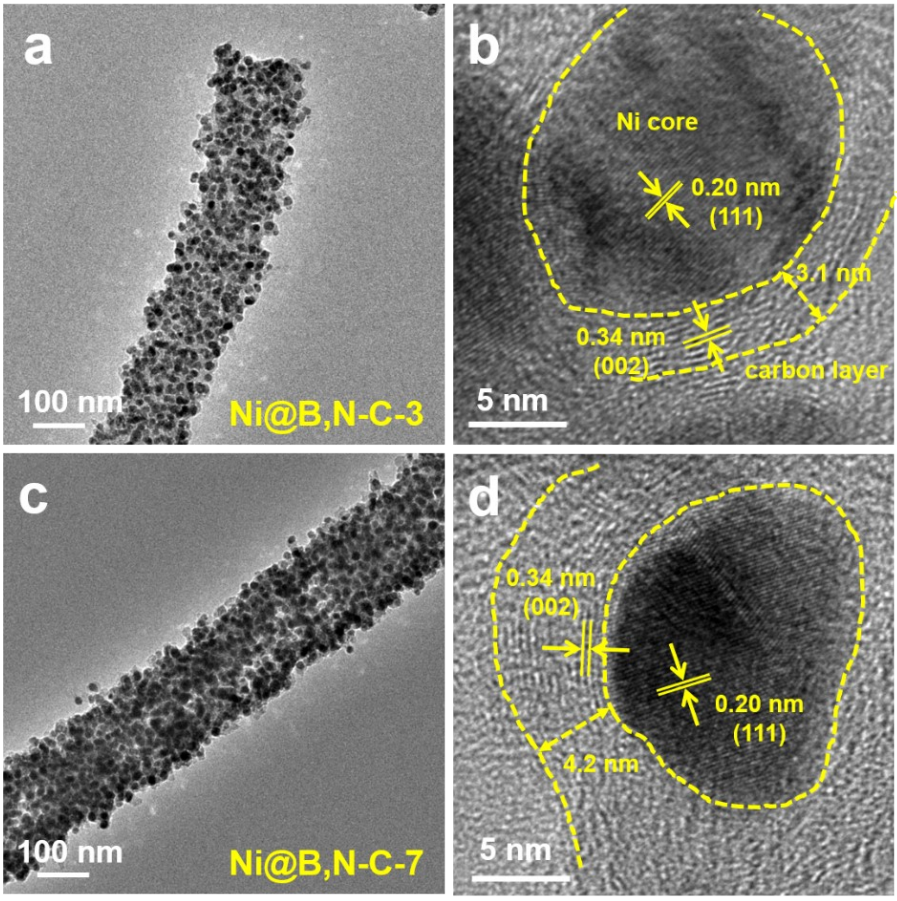

Fig. S8 (a) TEM and (b) HRTEM images of the Ni@B,N-C-3 NHs. (c) TEM and (d) HRTEM images of the Ni@B,N-C-7 NHs.

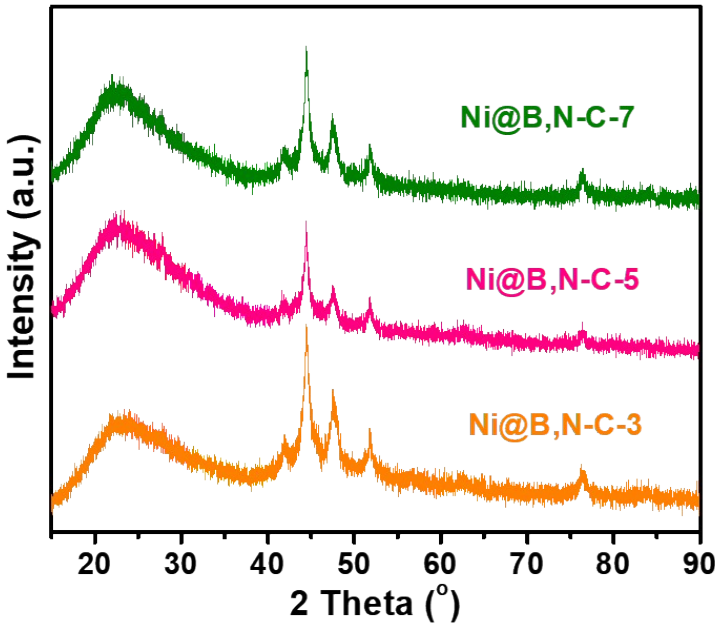

Fig. S9 XRD patterns of the Ni@B,N-C-3, Ni@B,N-C-5 and Ni@B,N-C-7 NHs.

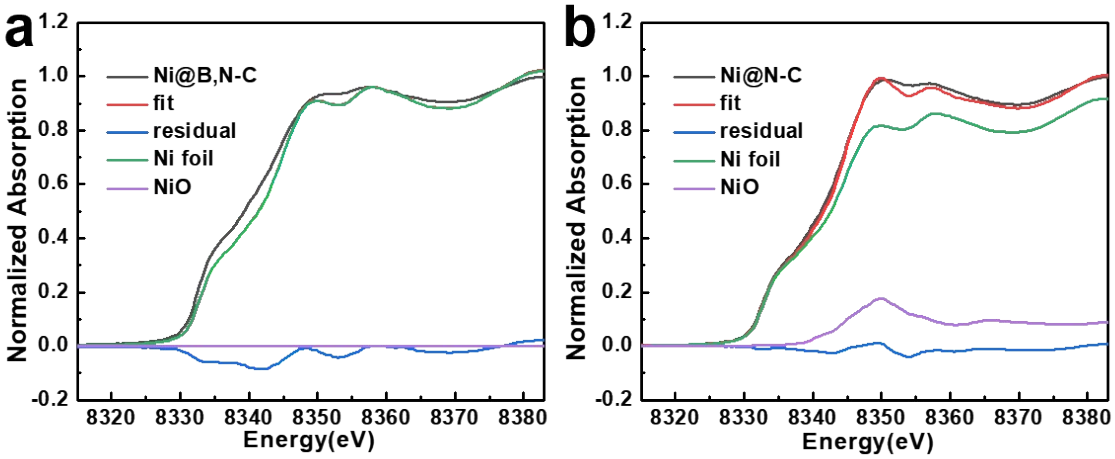

Fig. S10 Ni K-edge XANES spectra of the (a) Ni@B,N-C and (b) Ni@N-C NHs.

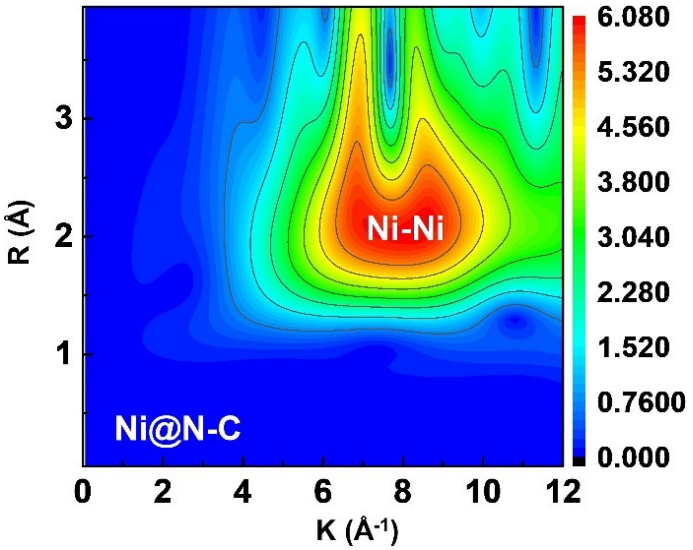

Fig. S11 Wavelet transform of the k^3-weighted EXAFS data at the Ni K-edge of the Ni@N-C NHs.

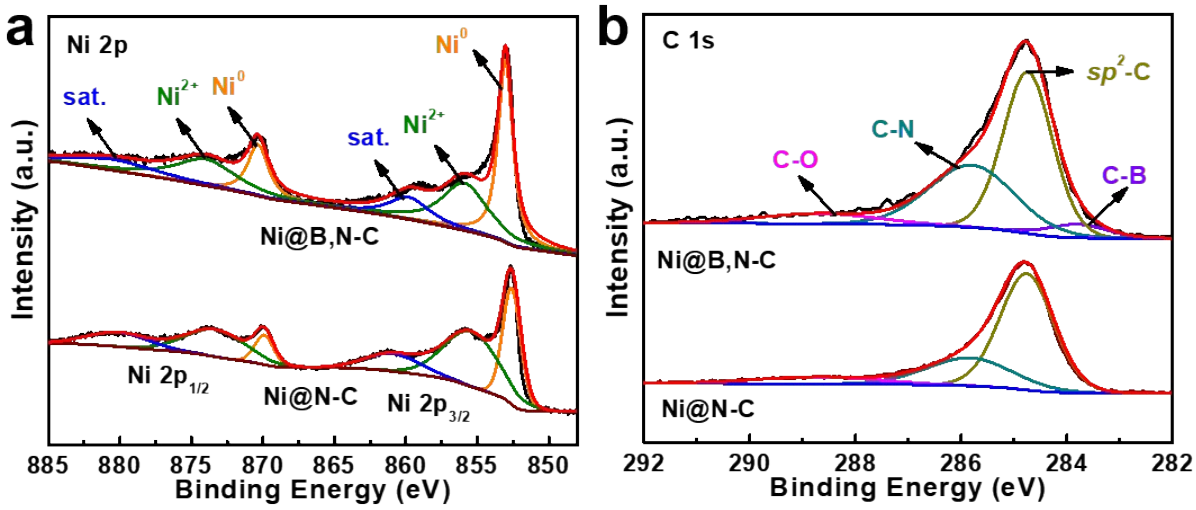

Fig. S12 (a) Ni 2p and (b) C 1s fine spectra for the Ni@B,N-C NHs and Ni@N-C NHs.

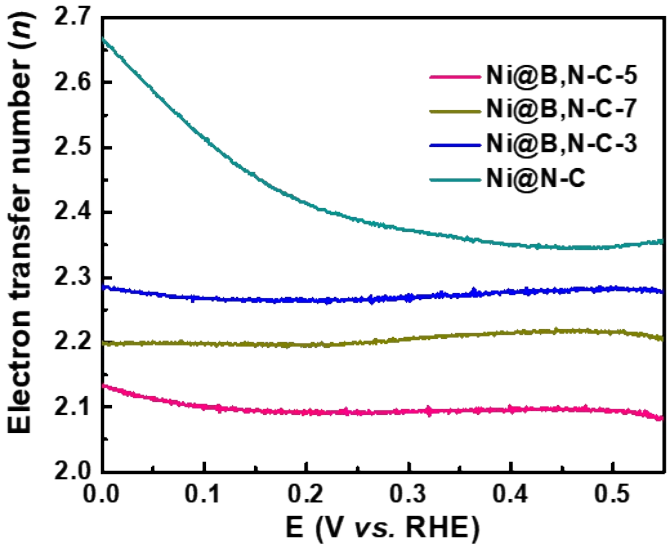

Fig. S13 Electron transfer number for the Ni@B,N-C-3, Ni@B,N-C-5, Ni@B,N-C-7 and Ni@N-C NHs.

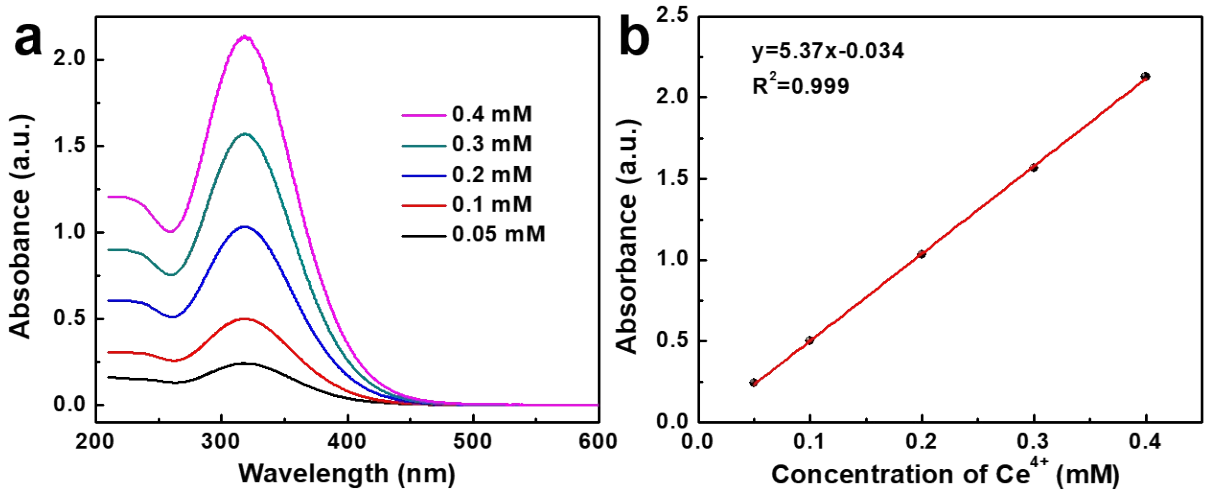

Fig. S14 (a) UV-vis spectra of Ce^{4+} solution with various concentrations and (b) its corresponding standard curve.

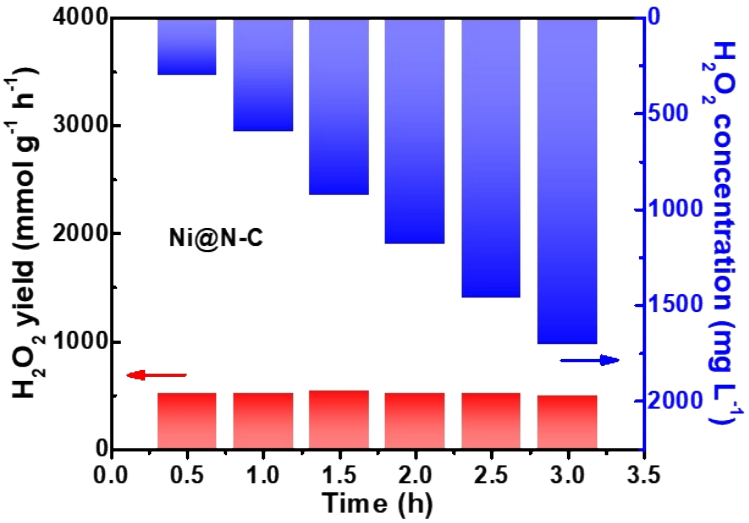

Fig. S15 Real-time production rate of H_2O_2 synthesis for the Ni@N-C NHs.

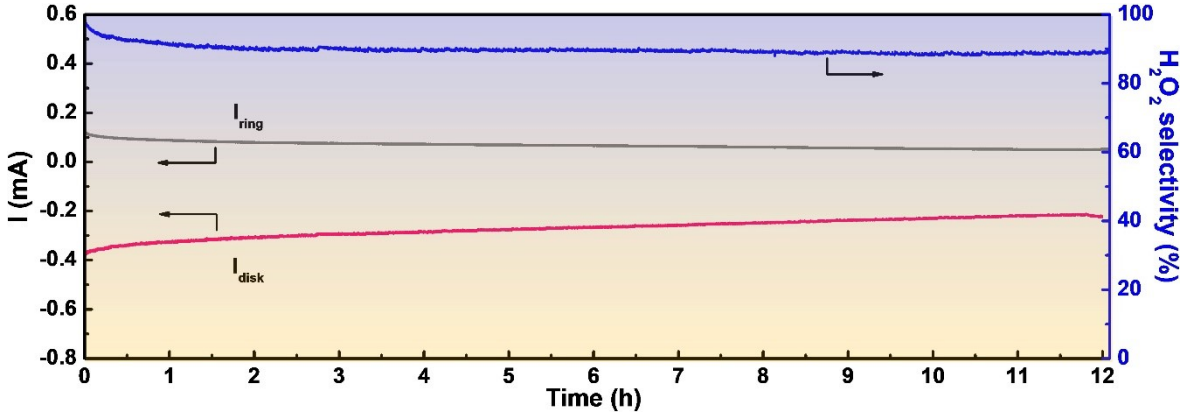

Fig. S16 Stability tests of Ni@B,N-C-5 at 0.2 V for 12 h.

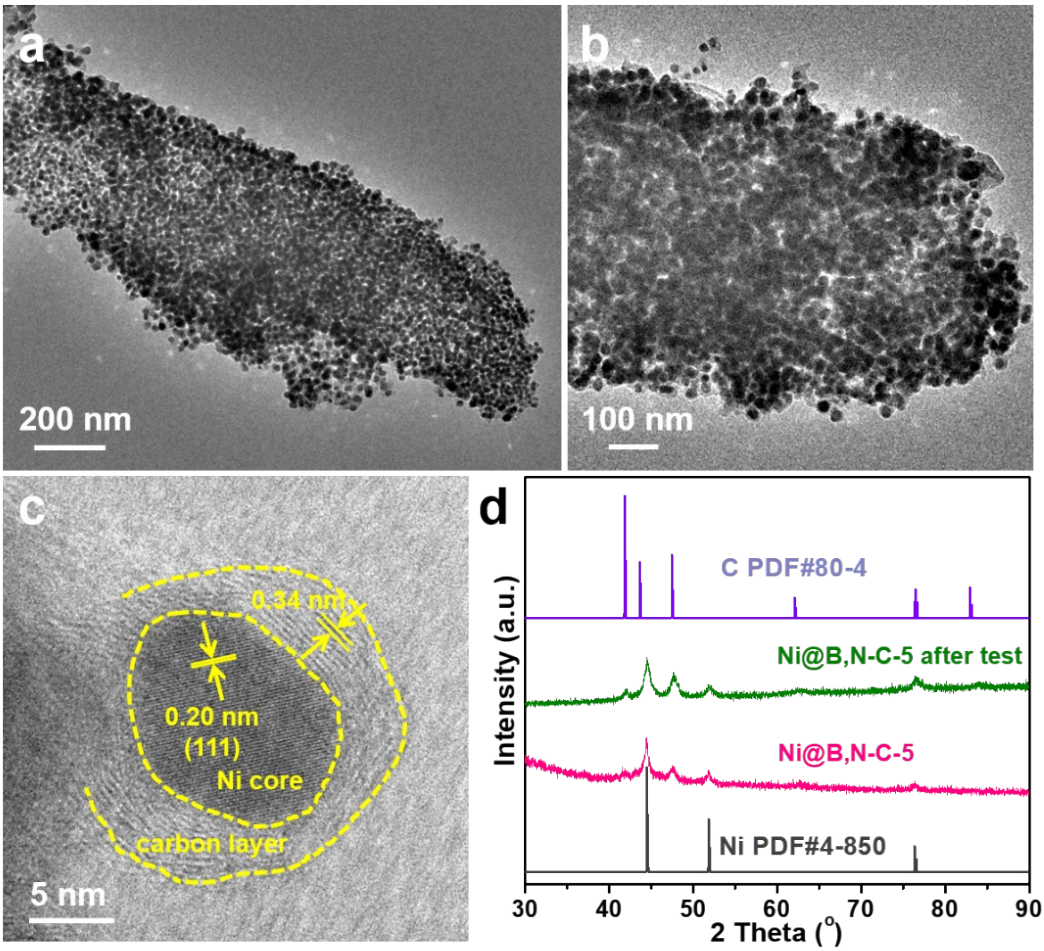

Fig. S17 (a, b) TEM, (c) HRTEM images and (d) XRD patterns for Ni@B,N-C-5 after long-term operation stability test.

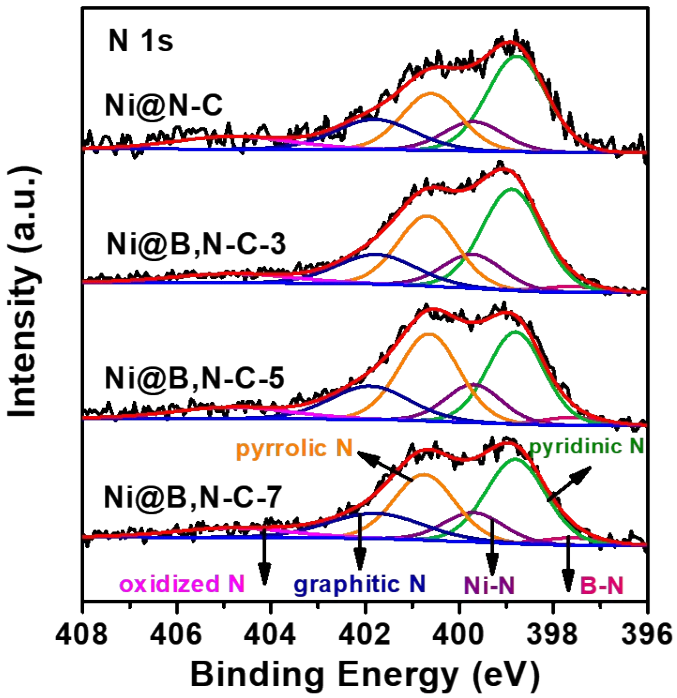

Fig. S18 N 1s fine spectra for the Ni@B,N-3, Ni@B,N-C-5, Ni@B,N-C-7 and Ni@N-C NHs.

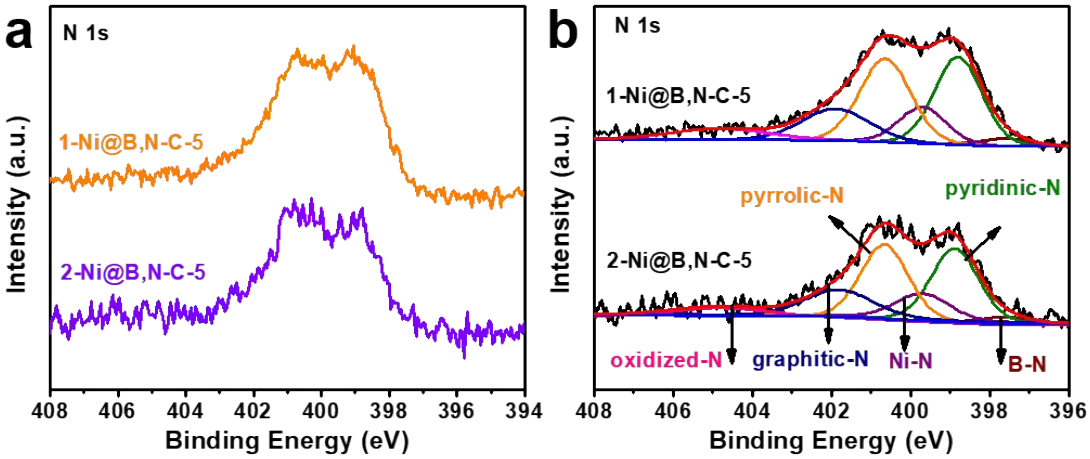

Fig. S19 N 1s XPS spectra of the Ni@B,N-C-5 NHs tested at different batches.

According to the integral calculation of XPS spectrum, the atomic percentage of N element is estimated to be 5.7% for the Ni@B,N-C-5 NHs. Based on the newly-obtained N 1s XPS spectrum (2-Ni@B,N-C-5), the contents of pyrrolic N and pyridinic N species were fitted to be 30.9% and 30.4%, respectively. This result is consisting with the original values (30.8% and 30.3% for the pyrrolic N and pyridinic N species, respectively), thereby confirming the influence of the doped boron atoms on nitrogen atomic configuration.

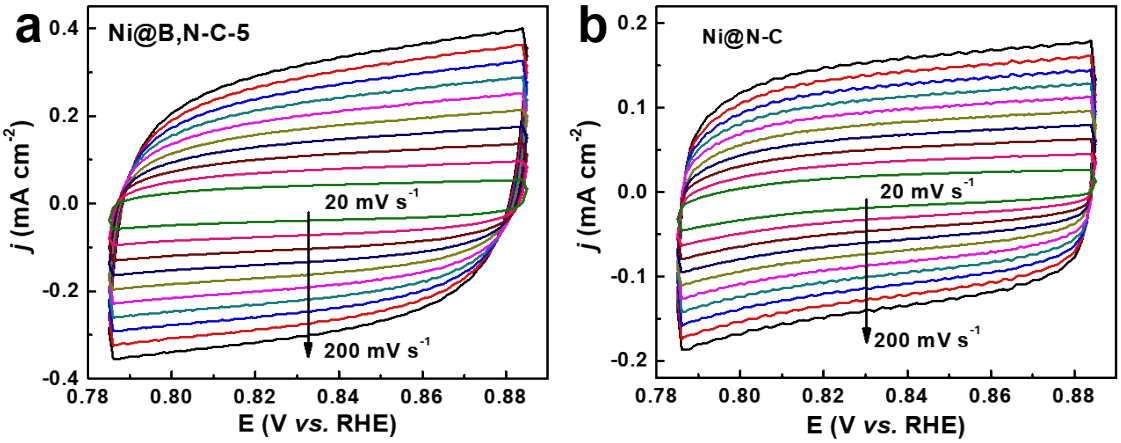

Fig. S20 Cyclic voltammogram curves with the scan rate ranging from 20 to 200 mV s^{-1} for the (a) Ni@B,N-C-5 and (b) Ni@N-C NHs in 0.1 M KOH.

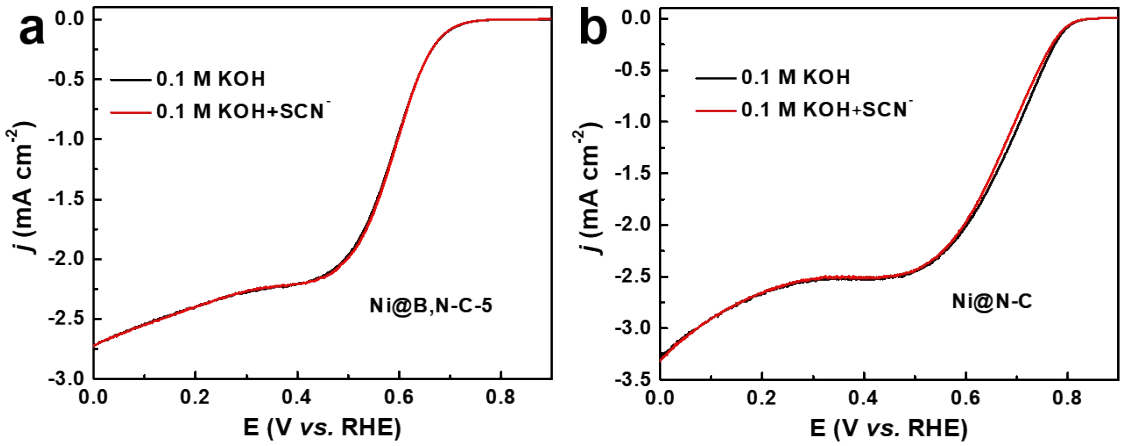

Fig. S21 LSV curves for SCN^- poisoning experiment on the (a) Ni@B,N-C-5 and (b) Ni@N-C NHs.

In consideration of the potential reaction between SCN^- and KOH, the rotating ring-disk electrode was unscrewed from the device and soaked in 10 mM NaSCN solution for 5 min. Then, the electrode was taken out from NaSCN solution while the residual SCN^- on the electrode surface was rinsed with deionized water, and the polarization curve was further measured in O_2-saturated 0.1 M KOH solution.

From Fig. S21, the LSV curves of Ni@B,N-C-5 and Ni@N-C NHs display no significant change before and after immersion in the NaSCN solution (10 mM), indicating that the Ni single-atom sites had little influence on the electrocatalytic $2e^-$ ORR activity of Ni@B,N-C-5 and Ni@N-C NHs.

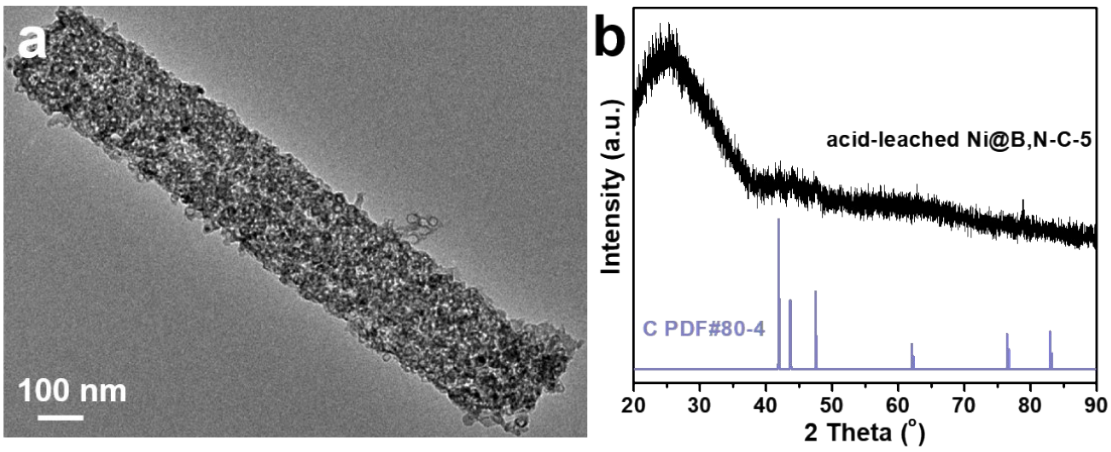

Fig. S22 (a) TEM image and (b) XRD pattern of the acid-leached Ni@B,N-C-5 NHs.

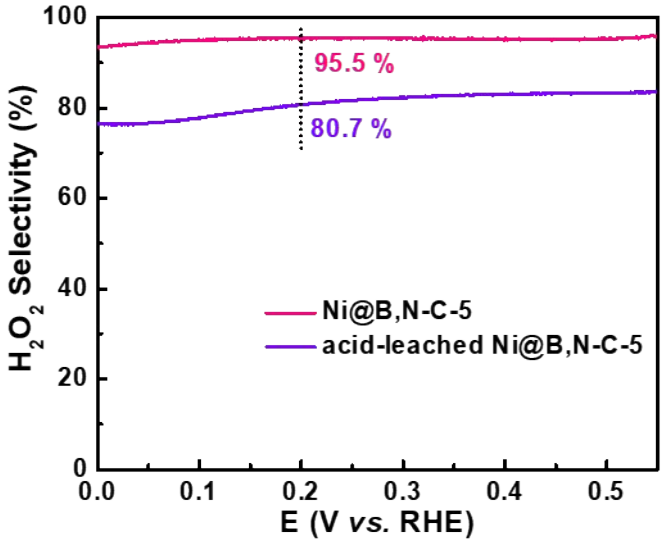

Fig. S23 Calculated H_2O_2 selectivity of the Ni@B,N-C-5 and acid-leached Ni@B,N-C NHs in O_2-saturated 0.1 M KOH at 1600 rpm.

In view of the co-existence of Ni NPs in Ni@B,N-C-5 NHs, the Ni@B,N-C-5 catalyst was further leached in a 2 M HCl solution at 40 °C for 12 h to remove the metallic Ni NPs. TEM and XRD characterizations in Fig. S22 show almost no residual NPs after acid leaching. The electrocatalytic $2e^-$ ORR activity of Ni@B,N-C-5 and acid-leached Ni@B,N-C-5 NHs was measured and compared, which apparently showed degraded $2e^-$ ORR activity in terms of the sharply reduced H_2O_2 selectivity from 95.5% to 80.7% (Fig. S23). This indicates that the metallic Ni NPs are beneficial for the high electrocatalytic activity of Ni@B,N-C-5 NHs.

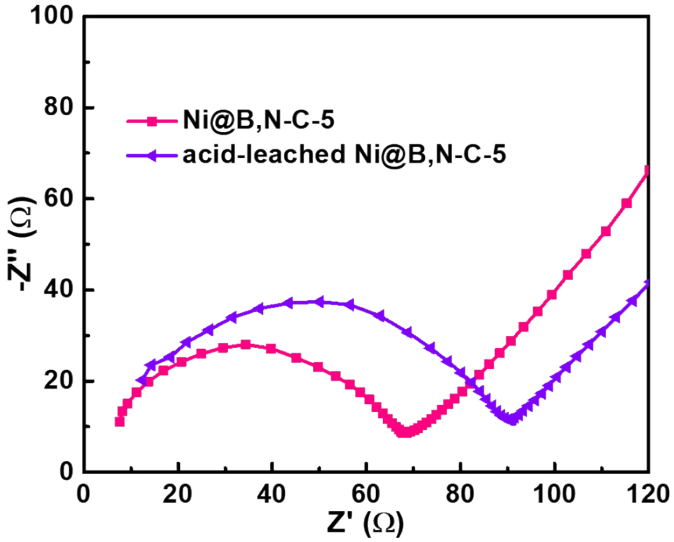

Fig. S24 Nyquist curves for the Ni@B,N-C-5 and acid-leached Ni@B,N-C-5 NHs measured at corresponding open circuit voltage under the actual ORR conditions.

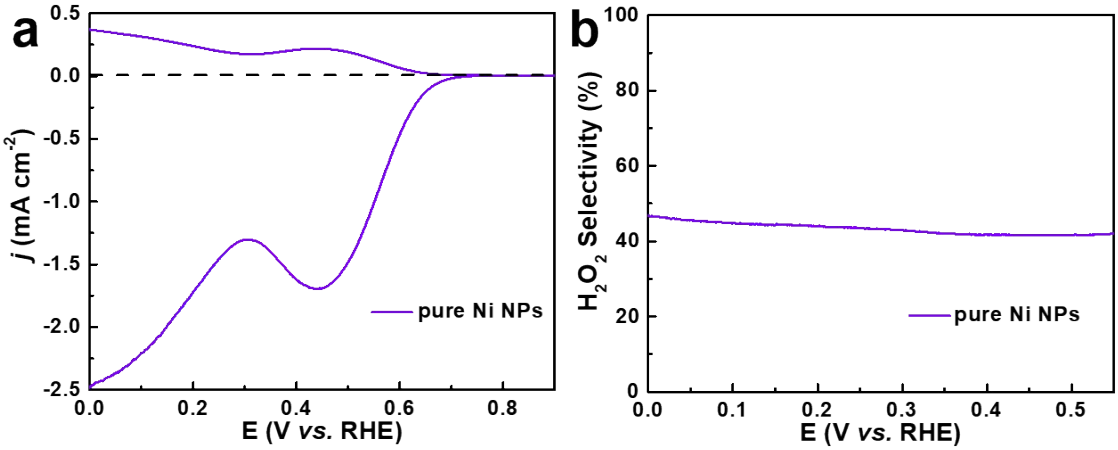

Fig. S25 (a) LSV and (b) calculated H_2O_2 selectivity of pure Ni nanoparticles in O_2-saturated 0.1 M KOH at 1600 rpm.

Further, EIS curves indicate that Ni@B,N-C-5 NHs also possess a smaller interfacial electron transfer resistance (69 Ω) than that of the acid-leached Ni@B,N-C-5 (93 Ω), demonstrating that the metallic core may serve as a conductive charge transport channel to accelerate the $2e^-$ ORR process (Fig. S24). Nevertheless, the pure Ni NPs exhibit a poor electrocatalytic H_2O_2 selectivity (Fig. S25). Give all in this, the B and N co-doped carbon shell plays an essential role in boosting the $2e^-$ ORR performance of the Ni@B,N-C-5 catalyst, whereas the Ni core may serve as an electron transfer channel to accelerate the electron migration.

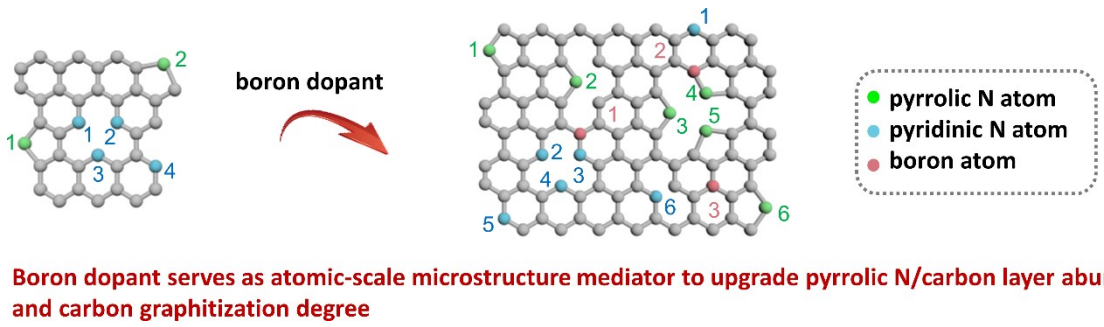

Fig. S26 Schematic illustration of the atomic-scale modulation effect of boron dopant on carbon layer.

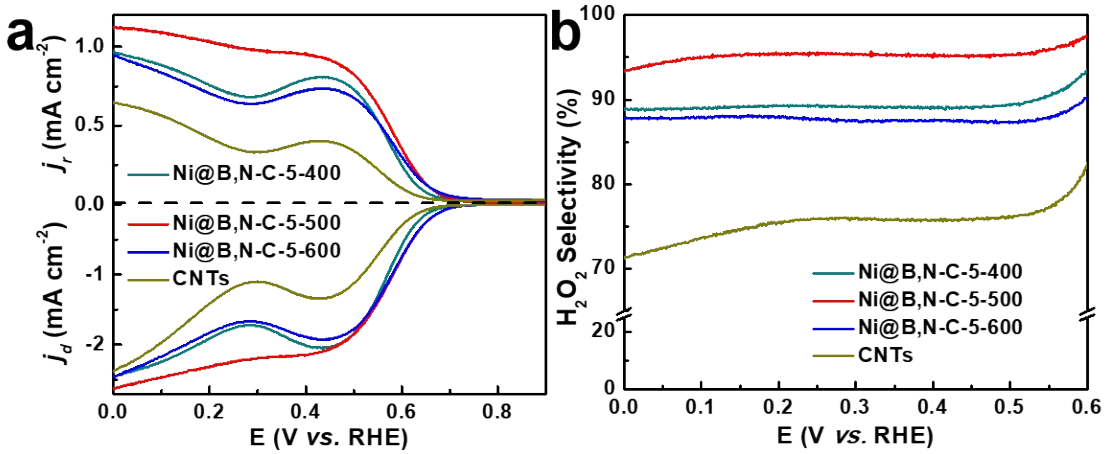

Fig. S27 (a) LSV curves and (b) H_2O_2 selectivity of the Ni@B,N-C-5-400, Ni@B,N-C-5-500 Ni@B,N-C-5-600 NHs and pure carbon nanotubes.

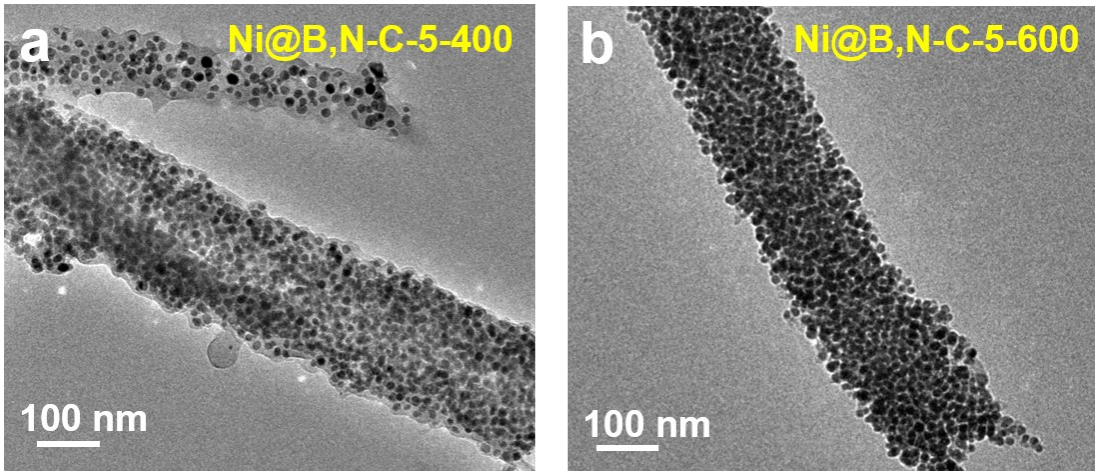

Fig. S28 TEM images for the (a) Ni@B,N-C-5-400 and (b) Ni@B,N-C-5-600 NHs.

Table S1. Summary and comparison of H_2O_2 production performance of some recently reported Ni- and carbon-based electrocatalysts.

Electrocatalysts	*Onset potential (vs. RHE)*	*H_2O_2 Selectivity*	*Faradaic efficiency*	*Electrolyte*	*Reference*
Ni@B,N-C	0.67 V	95.5 % @0.2 V	84 %	0.1 M KOH	This work
NiO_x-C	0.76 V	90.7 % @0.4 V	/	0.1 M KOH	1
NiN_x/C-AQNH$_2$	0.81 V	80 %	80 %	0.1 M KOH	2
COF-366-Ni	0.78 V	86 %	75 %	0.1 M KOH	3
Ni_3B	~ 0.65 V	~ 90 %	/	0.1 M KOH	4
Ni-N_2O_2/C	~ 0.72 V	> 90 %	85 %	0.1 M KOH	5
Ni-N-C	/	52 % @0.1 V	/	0.5 M H_2SO_4	6
NiOC	~0.50 V at 0.01 mA cm^{-2}	~ 89 % @0.2 V	/	0.1 M PBS	7
Ni-N-C-medium	/	76 % @0.58 V	/	0.1 M KOH	8
B-C	0.773 V	>85 %	85.1% in 1 M KOH	0.1 M KOH	9
B,N doped carbon	0.80 V @0.5 mA cm^{-2}	90 %	/	0.1 M KOH	10
BC-2-650	/	~95% at 0.55 V	74%	0.1 M KOH	11
N-mFLG-8	0.8 V	>95%	~100%	0.1 M KOH	12
Pyrr-N doped CNT-U-15T	/	93.5%	/	0.1 M KOH	13
NOC-6M	0.71 V @ 1 mA cm^{-2}	95.2%	92.4	0.1 M KOH	14

Table S2. Concentrations of nitrogen species from XPS in catalysts.

Catalysts	*B-N (%)*	*pyridinic N (%)*	*pyrrolic N (%)*	*Ni-N (%)*	*graphitic N (%)*	*oxidized N (%)*
Ni@N-C	/	38.8	22.8	11.9	16.4	10.1
Ni@B,N-C-3	2.2	37.7	25.8	12.6	14.7	7.0
Ni@B,N-C-5	2.7	30.3	30.8	12.6	15.7	7.9
Ni@B,N-C-7	2.8	34.0	27.1	11.9	16.4	7.8

Reference

[1] Z. Wu, T. Wang, J.-J. Zou, Y. Li, C. Zhang, *ACS Catal.* **2022**, *12*, 5911.

[2] X. Li, S. Tang, S. Dou, H. J. Fan, T. S. Choksi, X. Wang, *Adv. Mater.* **2021**, *34*, 2104891.

[3] C. Liu, H. Li, F. Liu, J. Chen, Z. Yu, Z. Yuan, C. Wang, H. Zheng, G. Henkelman, L. Wei, Y. Chen, *J. Am. Chem. Soc.* **2020**, *142*, 21861.

[4] F. Ma, S. Wang, X. Liang, C. Wang, F. Tong, Z. Wang, P. Wang, Y. Liu, Y. Dai, Z. Zheng, B. Huang, *Appl. Catal. B: Environ.* **2020**, *279*, 119371.

[5] Y. Wang, R. Shi, L. Shang, G. I. N. Waterhouse, J. Zhao, Q. Zhang, L. Gu, T. Zhang, *Angew. Chem. Int. Ed.* **2020**, *59*, 13057.

[6] Y. Sun, L. Silvioli, N. R. Sahraie, W. Ju, J. Li, A. Zitolo, S. Li, A. Bagger, L. Arnarson, X. Wang, T. Moeller, D. Bernsmeier, J. Rossmeis, F. Jaouen, P. Strasser, *J. Am. Chem. Soc.* **2019**, *141*, 12372.

[7] W. Xu, Z. Liang, S. Gong, B. Zhang, H. Wang, L. Su, X. Chen, N. Han, Z. Tian, T. Kallio, L. Chen, Z. Lu, X. Sun, *ACS Sustainable Chem. Eng.* **2021**, *9*, 7120.

[8] L. Shahcheraghi, C. Zhang, H.-J. Lee, M. Cusack-Striepe, F. Ismail, A. Abdellah, D. C. Higgins, *J. Phys. Chem. C* **2021**, *125*, 15830.

[9] Y. Xia, X. Zhao, C. Xia, Z.-Y. Wu, P. Zhu, J. Y. Kim, X. Bai, G. Gao, Y. Hu, J. Zhong, Y. Liu, H. Wang, *Nat. Commun.* **2021**, *12*, 4225.

[10] S. Chen, Z. Chen, S. Siahrostami, D. Higgins, D. Nordlund, D. Sokaras, T. Kim, Y. Liu, X. Yan, E. Nilsson, R. Sinclair, J. K. Nørskov, T. F. Jaramillo, Z. Bao, *J. Am. Chem. Soc.* **2018**, *140*, 7851.

[11] Y. Chang, J. Li, J. Ma, Y. Liu, R. Xing, Y. Wang, G. Zhang, *Sci. China Mater.* **2022**, *65*, 1276-1284.

[12] L. Li, C. Tang, Y. Zheng, B. Xia, X. Zhou, H. Xu, S. Z. Qiao, *Adv. Energy Mater.* **2020**, *10*, 2000789.

[13] J. Wan, G. Zhang, H. Jin, J. Wu, N. Zhang, B. Yao, K. Liu, M. Liu, T. Liu, L. Huang, *Carbon* **2022**, *191*, 340-349.

[14] C. Zhang, G. Liu, B. Ning, S. Qian, D. Zheng, L. Wang, *Int. J. Hydrogen Energy,* **2021**, *46*, 14277-14287.